AAS 16-530

IMPROVED MANEUVER-FREE APPROACH TO ANGLES-ONLY NAVIGATION FOR SPACE RENDEZVOUS

Joshua Sullivan[*], **Adam W. Koenig**[†], **Simone D'Amico**[‡]

This work introduces a novel strategy for improving angles-only relative navigation for distributed space systems. Instead of relying on orbit or attitude maneuvers to reconcile the known observability issues, a rigorous state comparison and observability assessment is conducted to provide new insight into the benefits gained from improved dynamic and measurement modeling. First of all, a new method is described to derive a J_2-perturbed state transition matrix in mean quasi-nonsingular relative orbit elements. In particular, Floquet theory is used to solve the resulting set of time-varying, periodic differential equations under the assumption of small state components. The presented formulation enables the seamless derivation of computationally efficient state transition matrices valid for different regimes of orbit eccentricity (from near-circular to arbitrary). Second, this research shows how the inclusion of nonlinearities in the measurement model vastly improves the condition number of the system's observability Gramian by increasing the accuracy of modeled bearing measurements. The results of this assessment lead to the design of a novel architecture for angles-only relative navigation which is comprised of an initial batch relative orbit determination algorithm used to initialize a sequential extended Kalman filter. The initialization method leverages the relative orbital element description to decouple the range uncertainty from the observable relative geometry, and a series of navigation filters are built using different combinations of the derived dynamics and measurement models. The prototype navigation algorithms are tested and validated in high-fidelity simulations which show that improved dynamics modeling has little effect on observability, whereas preserving nonlinearities in the measurement model reconciles the range ambiguity issues without necessarily requiring maneuvers.

INTRODUCTION

This paper presents a new analytical architecture for assessing and improving angles-only relative navigation capabilities for distributed space systems (DSS). A novel navigation filter concept which relies solely on camera-based bearing measurements is developed and validated. In particular, this research focuses on a systematic approach to assess and achieve accurate relative vision-based navigation without requiring maneuvers to remedy the known observability issues. Its development is largely motivated by the need to provide relative navigation capability using simple sensors for future classes of DSS missions including on-orbit servicing, autonomous rendezvous, and distributed aperture science instruments. The capability to accurately and robustly navigate with respect to other space resident objects using only a passive, high dynamic-range camera presents a distinct advantage over systems which make use of active, heavy, and/or expensive metrology such as radar and lidar. The long-term goal of this work is to meet the requirements posed by advanced DSS concepts such as mSTAR[1] and mDOT[2] under development at Stanford University. mSTAR is planned for launch in 2020, and will demonstrate fully autonomous vision-based rendezvous of a microsatellite (100 kg) with a non-cooperative nanosatellite ($<$10 kg) ejected in Low Earth Orbit (LEO). mDOT is a proposed technology demonstrator in a highly elliptical earth orbit intended to validate the performance of starshades for future

[*]Doctoral Candidate, Stanford University, Department of Aeronautics and Astronautics, Space Rendezvous Laboratory, Durand Building, 496 Lomita Mall, Stanford, CA 94305-4035

[†]Doctoral Candidate, Stanford University, Department of Aeronautics and Astronautics, Space Rendezvous Laboratory, Durand Building, 496 Lomita Mall, Stanford, CA 94305-4035

[‡]Assistant Professor, Stanford University, Department of Aeronautics and Astronautics, Space Rendezvous Laboratory, Durand Building, 496 Lomita Mall, Stanford, CA 94305-4035

exoplanet imaging missions. In preparation for the mSTAR mission, the work of this paper proceeds under the assumption of near-circular orbits. However, the outputs from this study provide an insightful analytical framework for future extension to eccentric orbits and new mission applications such as mDOT.

Angles-only navigation poses a difficult problem in state estimation due to the well-documented observability issues arising from the limitations of bearing angle measurements. The extensive research done by Woffinden and Geller[3] presents closed-form sufficient conditions for observability when using a linearized relative motion model in rectilinear coordinates. Contrary to the work presented here, the authors offer a solution that makes use of at least one translation maneuver to produce a detectable variation of the line-of-sight trend which resolves the observability issue.[4] Recently, Christensen and Geller explored the observability benefits produced by rotational maneuvers with the camera offset from the spacecraft center of gravity.[5] The results indicate that the state can be reconstructed with reasonable accuracy, but only for the cases of close proximity operation with inter-satellite range on the order of tens of meters. Several other approaches have focused on using higher-order and fully nonlinear models of relative rectilinear motion, but observability claims are only discussed under certain geometric conditions.[6,7,8] There has also been a growing interest in using the relationships developed between the rectilinear state and orbital element descriptions for applications in angles-only navigation. Schmidt[9] uses a set of relative orbital elements (ROE) built from the integration constants of the Hill-Clohessy-Wiltshire (HCW) equations[10] to argue that the relative motion shape and orientation are observable, leaving only an ambiguity in the scaling of the observed motion. Similarly, Gaias[11] studied the observability of the angles-only navigation problem using a distinctly different ROE state built from quasi-nonsingular orbital element differences.[12] In that work, the authors numerically confirm that the relative orbit shape and orientation are observable and conveniently captured by the relative semi-major axis and relative eccentricity/inclination vectors, and that the unobservability is confined to the relative mean argument of latitude. The mean inter-satellite separation is well-approximated as a function of the relative mean argument of latitude, confirming the intuition that the observed relative motion magnitude is scaled by the separation. The authors also present a numerical assessment of observability including the earth oblateness (J_2) perturbation and a novel maneuver-planning methodology for improving observability. The clear trend in angles-only navigation research has been to improve upon the dynamics modeling by incorporating higher-order solutions, different state representations, and/or perturbations in an attempt to improve observability. Instead, there is a lack of research studies that focus on the observability benefits gained from leveraging an improved measurement model that incorporates nonlinearities, particularly in the cases where curvilinear and ROE states are used. This research addresses this deficiency by combining advanced linear dynamics models with rigorously improved measurement models to construct a new angles-only navigation architecture.

This introduction is followed by a description of the three relevant dynamics models used to parameterize the relative motion, including a new method to derive the State Transition Matrix (STM) which describes the J_2-perturbed dynamics of the mean quasi-nonsingular ROE state. The subsequent section provides formulations of the measurement models which relate the observed bearing angles to the state. Next, the dynamics and measurement models of the previous sections are incorporated into a comprehensive observability assessment. This is followed by the development of a novel approach to initial relative orbit determination based on the observable relative orbit geometry, which acts in conjunction with the results of the observability assessment to inform the design of a complete angles-only navigation filter. The key navigation algorithms are described and validated in the subsequent section. Finally, the paper ends with a discussion of the lessons learned and contributions to the state-of-the-art, as well as a proposal of the way forward.

DYNAMIC MODELS

The objective of the angles-only navigation problem is the estimation of the motion of the target with respect to the servicer spacecraft from a set of bearing angle measurements. A rigorous formulation of this problem requires a dynamic model and a measurement model. The dynamic model describes how the state evolves over time. Here, only linear dynamic models are considered because they are well-suited for onboard implementation, simple, and facilitate inclusion of perturbations such as earth oblateness J_2 effects. While Lovell and Lee have shown observability improvements using fully nonlinear dynamics and measurement models,[6] the intent of this research is to achieve superior results through simpler models. The dynamic

models considered are of the form

$$\delta\boldsymbol{x}(t+\tau) = \boldsymbol{\Phi}(t,\tau)\delta\boldsymbol{x}(t) \tag{1}$$

where the state at time t, denoted $\delta\boldsymbol{x}(t)$, is related to the state at an arbitrary time $t+\tau$ by the STM, $\boldsymbol{\Phi}(t,\tau)$. The states used by previous authors can be divided into two broad categories: states defined through the relative position and velocity of the target, and states defined as functions of the Keplerian orbital elements of the servicer and target as described in the following.

Rectilinear State Dynamic Model

The most elementary state parameterization includes the relative position and velocity defined in a rotating reference frame centered about the servicer spacecraft. In this reference frame, the x-axis is aligned with the zenith (R) direction, the z-axis is aligned with the angular momentum of the servicer's orbit (N) direction, and the y-axis is aligned with the servicer's flight (T) direction, completing the right-handed RTN triad. The rectilinear state, $\delta\boldsymbol{x}_{rect}$, is given by

$$\delta\boldsymbol{x}_{rect} = \begin{pmatrix}\boldsymbol{\rho}_{rect} & \dot{\boldsymbol{\rho}}_{rect}\end{pmatrix}^T = \begin{pmatrix}\delta x & \delta y & \delta z & \delta\dot{x} & \delta\dot{y} & \delta\dot{z}\end{pmatrix}^T \tag{2}$$

where δx, δy, and δz, denote the R, T, and N components of the relative position vector. A well-known STM for relative position and velocity in the RTN frame is given for orbits of arbitrary eccentricity by Yamanaka and Ankersen.[13] However, for formations in unperturbed, near-circular orbits such that the separation is small relative to the orbit radius, the dynamics are well modeled using the STM of the HCW equations given by Alfriend,[14] which takes the form

$$\boldsymbol{\Phi}_{HCW}(t,\tau) = \begin{bmatrix} 4-3c_{n\tau} & 0 & 0 & \frac{s_{n\tau}}{n} & \frac{2-c_{n\tau}}{n} & 0 \\ -6n\tau-6s_{n\tau} & 1 & 0 & \frac{-2+2c_{n\tau}}{n} & \frac{4s_{n\tau}}{n}-3\tau & 0 \\ 0 & 0 & c_{n\tau} & 0 & 0 & \frac{s_{n\tau}}{n} \\ 3ns_{n\tau} & 0 & 0 & c_{n\tau} & 2s_{n\tau} & 0 \\ -6n+6nc_{n\tau} & 0 & 0 & -2s_{n\tau} & 0 & 0 \\ 0 & 0 & -ns_{n\tau} & 0 & 0 & c_{n\tau} \end{bmatrix} \tag{3}$$

where n denotes the mean motion of the servicer orbit and s and c denote the sine and cosine, respectively, of the argument in the subscript.

Curvilinear State Dynamic Model

In order to capture the curvature of spacecraft orbits, the relative position and velocity can instead be defined through curvilinear coordinates. The curvilinear state includes the difference in orbit radius, δr, angular in-plane separation, θ, angular out-of-plane separation, ϕ, and their respective rates. For dimensional consistency, the angular separations are multiplied by the orbit semi-major axis when applied to near-circular orbits. Thus, the curvilinear state is given as

$$\delta\boldsymbol{x}_{curv} = \begin{pmatrix}\boldsymbol{\rho}_{curv} & \dot{\boldsymbol{\rho}}_{curv}\end{pmatrix}^T = \begin{pmatrix}\delta r & a\theta & a\phi & \delta\dot{r} & a\dot{\theta} & a\dot{\phi}\end{pmatrix}^T \tag{4}$$

For clarity, the relationship between the the curvilinear coordinates and the absolute position, $\boldsymbol{r}$, of each spacecraft is illustrated in Figure 1. Hereafter, properties of the servicer are denoted by subscript s and properties of the target are denoted by subscript t. The dynamics of the curvilinear and rectilinear states are identical in near-circular orbits to first order,[15] so the state can be propagated using the STM in Equation 3.

ROE State Dynamic Model

Instead of using relative position and velocity, the state can be parameterized as a function of the absolute orbital elements of the spacecraft. This paper uses the ROE state defined by D'Amico,[12] which is given by

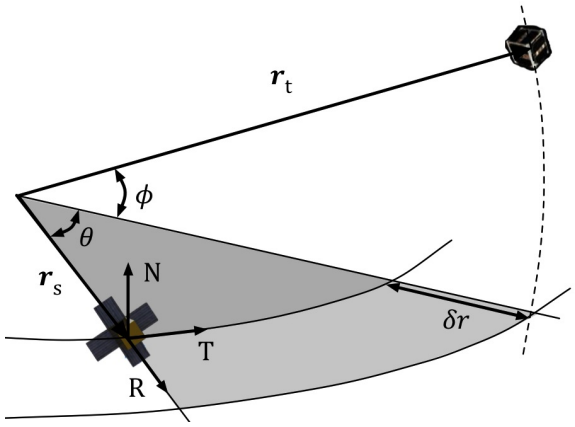

Figure 1: Illustration of curvilinear coordinate components.

the following difference of quasi-nonsingular orbital elements

$$\delta \boldsymbol{x}_{ROE} = \begin{pmatrix} \delta a \\ \delta \lambda \\ \delta \boldsymbol{e} \\ \delta \boldsymbol{i} \end{pmatrix} = \begin{pmatrix} \delta a \\ \delta \lambda \\ \delta e_x \\ \delta e_y \\ \delta i_x \\ \delta i_y \end{pmatrix} = \begin{pmatrix} (a_t - a_s)/a_s \\ (M_t - M_s) + (\omega_t - \omega_s) + c_{i_s}(\Omega_t - \Omega_s) \\ e_t c_{\omega_t} - e_s c_{\omega_s} \\ e_t s_{\omega_t} - e_s s_{\omega_s} \\ i_t - i_s \\ s_{i_s}(\Omega_t - \Omega_s) \end{pmatrix} \tag{5}$$

where a, e, i, ω, Ω, and M are the classical Keplerian elements. In this parameterization, δa is the relative semi-major axis, $\delta\lambda$ is the relative mean longitude, $\delta \boldsymbol{e}$ is the relative eccentricity vector, and $\delta \boldsymbol{i}$ is the relative inclination vector. The relative position, and thus the modeled bearing angles, can be computed from this state using simple transformations that will be discussed in the later sections. The relative eccentricity and inclination vectors may also be expressed in polar notation as

$$\begin{pmatrix} \delta e_x \\ \delta e_y \end{pmatrix} = \delta e \begin{pmatrix} c_\varphi \\ s_\varphi \end{pmatrix} \qquad \begin{pmatrix} \delta i_x \\ \delta i_y \end{pmatrix} = \delta i \begin{pmatrix} c_\vartheta \\ s_\vartheta \end{pmatrix} \tag{6}$$

The parameters φ and ϑ represent the pericenter and ascending node of the relative orbital motion described in the following section. For unperturbed Keplerian orbits, the STM for this state is given by D'Amico[12] as

$$\boldsymbol{\Phi}_{ROE}(t,\tau) = \begin{bmatrix} 1 & 0 & 0 & 0 & 0 & 0 \\ -1.5n\tau & 1 & 0 & 0 & 0 & 0 \\ 0 & 0 & 1 & 0 & 0 & 0 \\ 0 & 0 & 0 & 1 & 0 & 0 \\ 0 & 0 & 0 & 0 & 1 & 0 \\ 0 & 0 & 0 & 0 & 0 & 1 \end{bmatrix} \tag{7}$$

Here, n is the servicer mean motion. State definitions based on the orbital elements of the spacecraft allow for simple incorporation of perturbations such as earth oblateness J_2 effects into the dynamic model. The J_2 perturbation causes short- and long-period oscillations as well as secular drifts in the orbital elements. For simplicity, the oscillations due to J_2 are neglected in the dynamic model and are instead included in the measurement models described in the following section. The secular drifts in the mean orbital elements[14] are given as

$$\begin{pmatrix} \dot{M} \\ \dot{\omega} \\ \dot{\Omega} \end{pmatrix} = \frac{\gamma}{a^{7/2}\eta^4} \begin{pmatrix} \eta(3c_i^2 - 1) \\ 5c_i^2 - 1 \\ -2c_i \end{pmatrix} \qquad \gamma = \frac{3}{4} J_2 R_e^2 \sqrt{\mu} \qquad \eta = \sqrt{1 - ||\boldsymbol{e}||^2} \tag{8}$$

where μ is earth's gravitational parameter and R_e is the equatorial radius. Noting that only M, ω, and Ω are time-varying, the time derivates of the mean ROE are given as

$$\begin{pmatrix} \delta\dot{a} \\ \delta\dot{\lambda} \\ \delta\dot{e}_x \\ \delta\dot{e}_y \\ \delta\dot{i}_x \\ \delta\dot{i}_y \end{pmatrix} = \begin{pmatrix} 0 \\ (\dot{M}_t - \dot{M}_s) + (\dot{\omega}_t - \dot{\omega}_s) + c_{i_s}(\dot{\Omega}_t - \dot{\Omega}_s) \\ -e_t\dot{\omega}_t s_{\omega_t} + e_s\dot{\omega}_s s_{\omega_s} \\ e_t\dot{\omega}_t c_{\omega_t} - e_s\dot{\omega}_s c_{\omega_s} \\ 0 \\ s_{i_s}(\dot{\Omega}_t - \dot{\Omega}_s) \end{pmatrix} \tag{9}$$

Substituting Equation 8 for each spacecraft into Equation 9 yields

$$\begin{aligned} \begin{pmatrix} \delta\dot{a} \\ \delta\dot{\lambda} \\ \delta\dot{e}_x \\ \delta\dot{e}_y \\ \delta\dot{i}_x \\ \delta\dot{i}_y \end{pmatrix} &= \frac{\gamma a_t^{-7/2}}{(1-||\boldsymbol{e}_t||^2)^2} \begin{pmatrix} 0 \\ \sqrt{1-||\boldsymbol{e}_t||^2}(3c_{i_t}^2-1) + (5c_{i_t}^2-1) - 2c_{i_t}c_{i_s} \\ -e_t s_{\omega_t}(5c_{i_t}^2-1) \\ e_t c_{\omega_t}(5c_{i_t}^2-1) \\ 0 \\ -2c_{i_t}s_{i_s} \end{pmatrix} \\ &- \frac{\gamma a_s^{-7/2}}{(1-||\boldsymbol{e}_s||^2)^2} \begin{pmatrix} 0 \\ (1+\sqrt{1-||\boldsymbol{e}_s||^2})(3c_{i_s}^2-1) \\ -e_s s_{\omega_s}(5c_{i_s}^2-1) \\ e_s c_{\omega_s}(5c_{i_s}^2-1) \\ 0 \\ -2c_{i_s}s_{i_s} \end{pmatrix} + \sqrt{\mu} \begin{pmatrix} 0 \\ a_t^{-3/2} - a_s^{-3/2} \\ 0 \\ 0 \\ 0 \\ 0 \end{pmatrix} \end{aligned} \tag{10}$$

which can be reformulated in terms of the ROE and servicer orbital elements using the following identities:

$$a_t = a_s(1+\delta a) \qquad e_t c_{\omega_t} = e_s c_{\omega_s} + \delta e_x \qquad e_t s_{\omega_t} = e_s s_{\omega_s} + \delta e_y \qquad i_t = i_s + \delta i_x \tag{11}$$

The J_2-perturbed plant matrix can be computed by taking the derivatives of Equation 10 with respect to each of the ROE evaluated at $\delta\boldsymbol{x}_{ROE} = \boldsymbol{0}$. It is evident that the partial derivatives with respect to $\delta\lambda$ and δi_y are all zero. The remaining partial derivatives are given as

$$\frac{\partial\delta\dot{\boldsymbol{x}}_{ROE}}{\partial\delta a} = \frac{7}{2}\kappa \begin{pmatrix} 0 \\ -EP - \frac{3n}{7\kappa} \\ e_y Q \\ -e_x Q \\ 0 \\ S \end{pmatrix} \qquad \frac{\partial\delta\dot{\boldsymbol{x}}_{ROE}}{\partial\delta i_x} = \kappa \begin{pmatrix} 0 \\ -FS \\ 5e_y S \\ -5e_x S \\ 0 \\ 2T \end{pmatrix} \tag{12}$$

$$\frac{\partial\delta\dot{\boldsymbol{x}}_{ROE}}{\partial\delta e_x} = \kappa \begin{pmatrix} 0 \\ e_x GFP \\ -4e_x e_y GQ \\ (1+4e_x^2 G)Q \\ 0 \\ -4e_x GS \end{pmatrix} \qquad \frac{\partial\delta\dot{\boldsymbol{x}}_{ROE}}{\partial\delta e_y} = \kappa \begin{pmatrix} 0 \\ e_y GFP \\ -(1+4e_y^2 G)Q \\ 4e_x e_y GQ \\ 0 \\ -4e_y GS \end{pmatrix} \tag{13}$$

where the following substitutions have been applied for clarity

$$\begin{aligned} e_x = e_s c_{\omega_s}; \qquad e_y = e_s s_{\omega_s}; \qquad \kappa = \frac{\gamma}{a_s^{7/2}\eta_s^4}; \qquad E = 1+\eta_s; \qquad F = 4+3\eta_s \\ G = \frac{1}{\eta_s^2}; \qquad P = 3c_{i_s}^2 - 1; \qquad Q = 5c_{i_s}^2 - 1; \qquad S = s_{2i_s}; \qquad T = s_{i_s}^2 \end{aligned} \tag{14}$$

These partial derivatives can be assembled to form the J_2-perturbed plant matrix, $\boldsymbol{A}(t)$, which is expressed as

$$\boldsymbol{A}(t) = \kappa \begin{bmatrix} 0 & 0 & 0 & 0 & 0 & 0 \\ -\frac{7}{2}EP - \frac{3n}{2\kappa} & 0 & e_x GFP & e_y GFP & -FS & 0 \\ \frac{7}{2}e_y Q & 0 & -4e_x e_y GQ & -(1+4e_y^2 G)Q & 5e_y S & 0 \\ -\frac{7}{2}e_x Q & 0 & (1+4e_x^2 G)Q & 4e_x e_y GQ & -5e_x S & 0 \\ 0 & 0 & 0 & 0 & 0 & 0 \\ \frac{7}{2}S & 0 & -4e_x GS & -4e_y GS & 2T & 0 \end{bmatrix} \tag{15}$$

Due to the explicit dependence on e_x and e_y, the plant matrix is time-varying and periodic. However, Floquet theory[16] can be used to identify a linear time-invariant system that satisfies

$$\delta\dot{\boldsymbol{x}}_{ROE} = \boldsymbol{A}(t)\delta\boldsymbol{x}_{ROE} \qquad \delta\boldsymbol{x}_{ROE} = \boldsymbol{Q}(t)\boldsymbol{z} \qquad \dot{\boldsymbol{z}} = \boldsymbol{D}\boldsymbol{z} \tag{16}$$

such that the new plant matrix $\boldsymbol{D}$ is time-invariant. The proper transformation is a rotation of the relative eccentricity vector by the mean argument of perigee of the servicer. Thus, the transformation matrix, $\boldsymbol{Q}(t)$, and its time derivative, $\dot{\boldsymbol{Q}}(t)$, are given as

$$\boldsymbol{Q}(t) = \begin{bmatrix} 1 & 0 & 0 & 0 & 0 & 0 \\ 0 & 1 & 0 & 0 & 0 & 0 \\ 0 & 0 & c_{\omega_s} & -s_{\omega_s} & 0 & 0 \\ 0 & 0 & s_{\omega_s} & c_{\omega_s} & 0 & 0 \\ 0 & 0 & 0 & 0 & 1 & 0 \\ 0 & 0 & 0 & 0 & 0 & 1 \end{bmatrix} \qquad \dot{\boldsymbol{Q}}(t) = \kappa Q \begin{bmatrix} 0 & 0 & 0 & 0 & 0 & 0 \\ 0 & 0 & 0 & 0 & 0 & 0 \\ 0 & 0 & -s_{\omega_s} & -c_{\omega_s} & 0 & 0 \\ 0 & 0 & c_{\omega_s} & -s_{\omega_s} & 0 & 0 \\ 0 & 0 & 0 & 0 & 0 & 0 \\ 0 & 0 & 0 & 0 & 0 & 0 \end{bmatrix} \tag{17}$$

The time-invariant plant matrix is related to the time-varying plant and transformation matrices by

$$\boldsymbol{D} = \boldsymbol{Q}^{-1}(t)(\boldsymbol{A}(t)\boldsymbol{Q}(t) - \dot{\boldsymbol{Q}}(t)) \tag{18}$$

and evaluating its exponential yields

$$e^{\boldsymbol{D}\tau} = \begin{bmatrix} 1 & 0 & 0 & 0 & 0 & 0 \\ (-\frac{7}{2}\kappa EP - \frac{3}{2}n)\tau & 1 & \kappa eFGP\tau & 0 & -\kappa FS\tau & 0 \\ 0 & 0 & 1 & 0 & 0 & 0 \\ -\frac{7}{2}\kappa eQ\tau & 0 & 4\kappa e^2 GQ\tau & 1 & -5\kappa eS\tau & 0 \\ 0 & 0 & 0 & 0 & 1 & 0 \\ \frac{7}{2}\kappa S\tau & 0 & -4\kappa eGS\tau & 0 & 2\kappa T\tau & 1 \end{bmatrix} \tag{19}$$

The J_2-perturbed STM, $\boldsymbol{\Phi}_{J_2}(t,\tau)$, is related to this exponential and the transformation matrix by

$$\boldsymbol{\Phi}_{J_2}(t,\tau) = \boldsymbol{Q}(t+\tau)e^{\boldsymbol{D}\tau}\boldsymbol{Q}^{-1}(t) =$$

$$\begin{bmatrix} 1 & 0 & 0 & 0 & 0 & 0 \\ -\frac{7}{2}\kappa EP\tau - \frac{3}{2}n\tau & 1 & \kappa e_{xi}FGP\tau & \kappa e_{yi}FGP\tau & -\kappa FS\tau & 0 \\ \frac{7}{2}\kappa e_{yf}Q\tau & 0 & c_{\Delta\omega} - 4\kappa e_{xi}e_{yf}GQ\tau & -s_{\Delta\omega} - 4\kappa e_{yi}e_{yf}GQ\tau & 5\kappa e_{yf}S\tau & 0 \\ -\frac{7}{2}\kappa e_{xf}Q\tau & 0 & s_{\Delta\omega} + 4\kappa e_{xi}e_{xf}GQ\tau & c_{\Delta\omega} + 4\kappa e_{yi}e_{xf}GQ\tau & -5\kappa e_{xf}S\tau & 0 \\ 0 & 0 & 0 & 0 & 1 & 0 \\ \frac{7}{2}\kappa S\tau & 0 & -4\kappa e_{xi}GS\tau & -4\kappa e_{yi}GS\tau & 2\kappa T\tau & 1 \end{bmatrix} \tag{20}$$

where the subscripts i and f denote initial and final values, respectively, of the components of the eccentricity vector of the servicer orbit and $\Delta\omega$ denotes the change in argument of perigee of the servicer orbit over the propagation time. Equation 20 presents an STM for the mean ROE in a J_2-perturbed orbit of arbitrary eccentricity derived under the single assumption that the individual components of $\delta\boldsymbol{x}_{ROE}$ are small for the duration of the propagation. Here, in contrast to the well known Gim-Alfriend STM,[17] the mean anomaly of the servicer and the relative mean longitude are employed. As a consequence, the elements of the second row are simple and less costly to compute.

The presented STM demonstrates that the relative mean longitude, eccentricity, and inclination are fully coupled when secular J_2 perturbations are included. However, these terms vary widely in magnitude for near-circular orbits. First, the terms proportional to e^2 are always small and can be reasonably neglected. Second,

the remaining terms proportional to e will be small compared to all other terms as long as the orbit is not equatorial or polar. Thus, an even simpler STM is derived by neglecting all terms dependent on eccentricity as given by

$$\mathbf{\Phi}^*_{J_2}(t,\tau) = \begin{bmatrix} 1 & 0 & 0 & 0 & 0 & 0 \\ -\frac{7}{2}\kappa EP\tau - \frac{3}{2}n\tau & 1 & 0 & 0 & -\kappa FS\tau & 0 \\ 0 & 0 & c_{\Delta\omega} & -s_{\Delta\omega} & 0 & 0 \\ 0 & 0 & s_{\Delta\omega} & c_{\Delta\omega} & 0 & 0 \\ 0 & 0 & 0 & 0 & 1 & 0 \\ \frac{7}{2}\kappa S\tau & 0 & 0 & 0 & 2\kappa T\tau & 1 \end{bmatrix} \tag{21}$$

which is identical to the matrix presented by Gaias[18] for near-circular orbits. This STM captures the precession of the relative eccentricity vector and the secular shift of the orbital planes as a function of the relative inclination due to the J_2 perturbation, which are also captured in the original STM derived by D'Amico[12] and used in the frame of the TanDEM-X[19] and PRISMA[20] formation-flying missions. Furthermore, this new matrix reveals additional terms which describe the secular variation of the relative mean longitude and a secular shift of the orbital planes occurring as a function of the relative semi-major axis. Therefore, the strongest variations in the relative motion due to J_2 occur when the two spacecraft have a large relative inclination and a large relative semi-major axis. Similar to the effect of proposed maneuver profiles given by previous authors, natural perturbation in the relative motion due to J_2 causes detectable variation in the observed bearing angles over time which can be leveraged to improve the system observability.

MEASUREMENT MODELS

It is now necessary to model the observed bearing angles as functions of the state variables. The general form of the nonlinear measurement model is given as

$$\boldsymbol{y} = \boldsymbol{h}(\delta\boldsymbol{x}, t) \tag{22}$$

where $\boldsymbol{y}$ is the vector of output measurements. Evaluation of the measurement function $\boldsymbol{h}$ depends on which state is being used.

Rectilinear Measurement Model

Before defining the bearing angles it is first necessary to define the camera frame. Since typical approaches to a space resident object start from large initial along-track separations,[1,21,22] a natural choice for a nominal camera orientation is in the (anti-)flight direction. (Anti-)parallel relative eccentricity and inclination vectors can be implemented to ensure that the formation maintains separation in the radial/cross-track motion, even under the presence of uncertainty in the along-track motion.[23] Accordingly, passively safe approach and receding trajectories can be achieved through small changes in the relative semi-major axis with no need to reorient the camera. For simplicity but without loss of generality, in this paper we consider a camera with fixed boresight alignment in the anti-flight direction. Under this assumption, the relative position vectors in the camera and RTN frames are related by

$$\boldsymbol{\rho}^c = \boldsymbol{R}^c_{RTN}\boldsymbol{\rho}^{RTN} = \begin{bmatrix} 1 & 0 & 0 \\ 0 & 0 & 1 \\ 0 & -1 & 0 \end{bmatrix} \boldsymbol{\rho}^{RTN} \tag{23}$$

The bearing angles (azimuth η and elevation ψ) can be expressed directly as functions of the rectilinear relative position vector in the camera frame, $\boldsymbol{\rho}^c$, as given by

$$\boldsymbol{h}(\delta\boldsymbol{x}_{rect}) = \begin{pmatrix} \eta \\ \psi \end{pmatrix} = \begin{pmatrix} \arcsin\left(\rho^c_y / ||\boldsymbol{\rho}^c||\right) \\ \arctan\left(\rho^c_x / \rho^c_z\right) \end{pmatrix} \tag{24}$$

The relationship between the bearing angles and the relative position is illustrated in Figure 2.

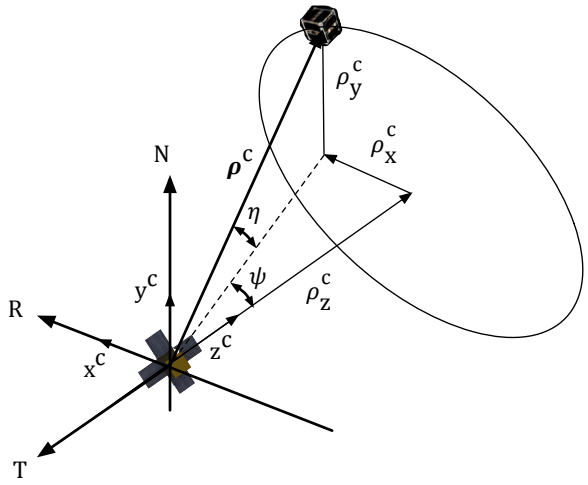

Figure 2: Relationship between relative position and bearing angles.

Curvilinear Measurement Model

The bearing angles for a curvilinear state are computed by mapping $\delta\boldsymbol{x}_{curv}$ to $\delta\boldsymbol{x}_{rect}$ and applying Equations 23 and 24. The mapping from curvilinear to rectilinear relative position is given by

$$\delta x = (a+\delta r)c_\theta c_\phi - a \qquad \delta y = (a+\delta r)s_\theta c_\phi \qquad \delta z = (a+\delta r)s_\phi \tag{25}$$

ROE Measurement Model

To compute the bearing angles as functions of the ROE state it is necessary to employ a map from the ROE to rectilinear relative position. In this paper, three different maps are considered: 1) linear map from ROE to rectilinear position, 2) linear map from ROE to curvilinear position, followed by nonlinear map to rectilinear position, and 3) nonlinear map from ROE to rectilinear position. Additionally, recall that the dynamic models described in the previous section include only the secular drift of the mean ROE due to J_2 and neglect the short- and long- period oscillations characterizing the osculating ROE. To address the difference between the mean and osculating ROE, this paper includes two sets of measurement models. In the first, the oscillations are neglected entirely and the relative position is computed from the mean ROE. In the second, the mean to osculating transformation described by Schaub[24] is applied to the ROE before the relative position is computed. This transformation is linear in J_2, but nonlinear in separation. The sequence of computations required for each of the six measurement models is illustrated in Figure 3. Hereafter, each measurement model will be denoted by the notation used in this figure (e.g. $\boldsymbol{y}_{1-6}$).

Linear Map to Rectilinear/Curvilinear: The linear map between the ROE and rectilinear or curvilinear states is formulated by treating the ROE elements as integration constants of the HCW equations.[12] The curvilinear state can subsequently be mapped to rectilinear relative position using Equation 25 if needed. The relationship between the ROE and translational states is given by

$$\delta\boldsymbol{x}_{curv/rect} \approx a \begin{bmatrix} 1 & 0 & -c_u & -s_u & 0 & 0 \\ 0 & 1 & 2s_u & -2c_u & 0 & 0 \\ 0 & 0 & 0 & 0 & s_u & -c_u \\ 0 & 0 & ns_u & -nc_u & 0 & 0 \\ -1.5n & 0 & 2nc_u & 2ns_u & 0 & 0 \\ 0 & 0 & 0 & 0 & nc_u & ns_u \end{bmatrix} \delta\boldsymbol{x}_{ROE} = \boldsymbol{T}(t)\delta\boldsymbol{x}_{ROE} \tag{26}$$

This map projects the ROE state into two orthogonal ellipses in the TR and TN planes. The oscillations in the R, T, and N directions are of magnitude $a\delta e$, $2a\delta e$, and $a\delta i$, respectively. These ellipses are offset by $a\delta a$ in the radial direction and by $a\delta\lambda$ in the along-track direction.

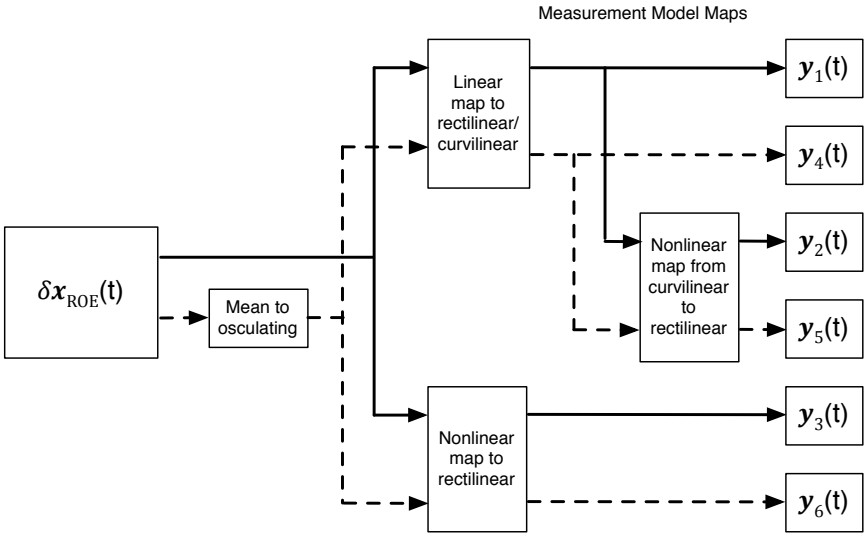

Figure 3: Computation sequence for each of the six considered ROE measurement models.

A snapshot of the geometric insight provided by this transformation is illustrated in Figure 4, where the drift of $a\delta\lambda$ due to $a\delta a$ is not shown for clarity. The choice of orienting the camera boresight in the anti-

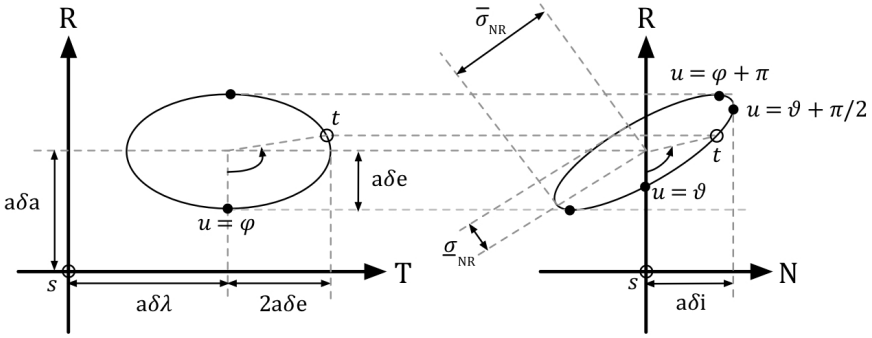

Figure 4: Relationship between ROE and relative position and velocity.

flight (-T) direction implies that the observed relative motion takes place in the NR plane. Accordingly, it is interesting to further analyze the implications of Equation 26 on the NR motion. The cross-track and radial position components are expressed in terms of the polar coordinates of the relative eccentricity and inclination vectors as

$$\begin{pmatrix} a\phi \\ \delta r \end{pmatrix} \approx \begin{pmatrix} \delta z \\ \delta x \end{pmatrix} = \begin{bmatrix} -a\delta i s_\vartheta & a\delta i c_\vartheta \\ -a\delta e c_\varphi & -a\delta e s_\varphi \end{bmatrix} \begin{pmatrix} \cos(u) \\ \sin(u) \end{pmatrix} + \begin{pmatrix} 0 \\ a\delta a \end{pmatrix} = \boldsymbol{M} \begin{pmatrix} \cos(u) \\ \sin(u) \end{pmatrix} + \begin{pmatrix} 0 \\ a\delta a \end{pmatrix} \tag{27}$$

Equation 27 is a parametric expression describing the tilted ellipse that traces out the NR motion. The $a\delta a$ term corresponds to an offset of the center of the NR ellipse along the R direction, while the size, shape, and orientation are compactly captured in the singular value decomposition (SVD) of the above matrix, $\boldsymbol{M}$. The SVD takes the following general form:

$$\boldsymbol{M} = \boldsymbol{U}\boldsymbol{\Sigma}\boldsymbol{V}^T \qquad \boldsymbol{U},\ \boldsymbol{\Sigma},\ \boldsymbol{V} \in \mathbb{R}^{2\times 2} \tag{28}$$

The two diagonal elements of $\boldsymbol{\Sigma}$ are the maximum and minimum singular values, $\overline{\sigma}_{NR}$ and $\underline{\sigma}_{NR}$, which geometrically capture the lengths of semi-major and semi-minor axes of the NR ellipse, respectively. The column of $\boldsymbol{U}$ corresponding to $\overline{\sigma}_{NR}$ describes the orientation of the semi-major axis in the NR plane. The

remaining column describes the orientation of the semi-minor axis, and is by definition orthogonal to the semi-major axis. The singular values are given as

$$\begin{aligned}\overline{\sigma}_{_{NR}} &= \frac{a}{\sqrt{2}}\left[\delta e^2+\delta i^2+\sqrt{\delta e^4+\delta i^4-2\delta e^2\delta i^2 c_{2(\varphi-\vartheta)}}\,\right]^{1/2}\\ \underline{\sigma}_{_{NR}} &= \frac{a}{\sqrt{2}}\left[\delta e^2+\delta i^2-\sqrt{\delta e^4+\delta i^4-2\delta e^2\delta i^2 c_{2(\varphi-\vartheta)}}\,\right]^{1/2}\end{aligned} \tag{29}$$

and the column of $\boldsymbol{U}$ corresponding to the semi-major axis orientation is given by

$$\begin{pmatrix}U_{11}\\U_{21}\end{pmatrix} = \begin{pmatrix}\dfrac{\sqrt{\delta e^4+\delta i^4-2\delta e^2\delta i^2 c_{2(\varphi-\vartheta)}}+\delta i^2-\delta e^2}{2\delta e\delta i s_{\varphi-\vartheta}}\\ 1\end{pmatrix} \tag{30}$$

If the relative semi-major axis is zero, the singular values can be interpreted as the magnitude of the maximum and minimum separation in the NR plane, the latter of which is a useful metric of passive safety. The minimum singular value is maximized for fixed δe and δi if φ and ϑ are separated by 0 or 180 degrees, in agreement with the relative eccentricity/inclination-vector separation concept developed by D'Amico.[23] Conversely, if φ and ϑ are separated by 90 degrees, the NR ellipse degenerates into a straight line.

It is important to note that Equation 30 demonstrates that the NR ellipse can be oriented with the semi-major axis sloping positively (as shown in Figure 4) or negatively in the NR plane, depending on the relative values of φ and ϑ. By imposing that U_{11} is positive, the semi-major axis slope is shown to be positive if the condition $s_{\varphi-\vartheta} < 0$ is satisfied. It is also possible to identify the direction in which the target spacecraft traverses the relative trajectory in the NR plane. Note that at the relative ascending node, where $u = \vartheta$, the cross-track separation is zero and the target is moving in the direction of positive cross-track displacement. The rotation direction of the relative motion can be inferred by the radial position with respect to the center of the NR ellipse. From Equation 27 it is found that the motion is counter-clockwise as in Figure 4 if the condition $c_{\varphi-\vartheta} > 0$ is satisfied.

From this analysis, it is clear that the observed relative motion in the NR plane can be assessed as a function of $a\delta a,\ a\delta\boldsymbol{e}$, and $a\delta\boldsymbol{i}$ only. These results provide improved geometric intuition to the radial and cross-track motion established by relative eccentricity/inclination-vector separation concept developed by D'Amico.[23] In the context of angles-only navigation, the implications of these results are twofold: (1) the relative shape and orientation of the NR motion is observable irrespective of the ambiguity in range, and (2) guidance strategies can be devised that build relative motion with passively safe minimum radial/cross-track separation even when there is uncertainty in the mean along-track separation.

Nonlinear Map to Rectilinear: The nonlinear map from ROE to relative position is accomplished by first using the ROE and the known absolute orbital elements of the servicer to calculate the absolute orbital elements of the target. The absolute position and velocity of the servicer and target are then computed from their respective absolute orbital elements. Finally, from these values the relative position is computed in the RTN frame centered at the servicer.

OBSERVABILITY ANALYSIS

It is well documented in literature that the angles-only navigation problem is not fully observable for purely linear models of the relative position evolution. However, the aforementioned work of Lovell and Lee[6] has also proven that the state is locally weak observable for formations satisfying certain geometric constrains through the use of Lie derivatives with full nonlinear dynamics and measurement models. Additionally, Gaias has demonstrated that inclusion of J_2 effects in the measurement model leads to full observability, but with a poor condition number.[11] This suggests that inclusion of nonlinearities in the dynamic and measurement models is critical in order to achieve full observability in the maneuver-free angles-only navigation problem. Accordingly, the following analysis is used to identify which of our proposed models maximizes observability and minimizes computational cost. Consider a state trajectory passing through $\delta\boldsymbol{x}(t_0)$ at time t_0 with p

measurements taken at times t_1 through t_p. The measurement vector, $\boldsymbol{Y}$, for this scenario is given by

$$\boldsymbol{Y} = \begin{pmatrix} \boldsymbol{y}(t_1) \\ \boldsymbol{y}(t_2) \\ \vdots \\ \boldsymbol{y}(t_p) \end{pmatrix} = \begin{pmatrix} \boldsymbol{h}(\boldsymbol{\Phi}(t_0,\tau_1)\delta\boldsymbol{x}(t_0),t_1) \\ \boldsymbol{h}(\boldsymbol{\Phi}(t_0,\tau_2)\delta\boldsymbol{x}(t_0),t_2) \\ \vdots \\ \boldsymbol{h}(\boldsymbol{\Phi}(t_0,\tau_p)\delta\boldsymbol{x}(t_0),t_p) \end{pmatrix} \tag{31}$$

To demonstrate local observability about this trajectory, it is sufficient to demonstrate that the matrix of partial derivatives of the measurements with respect to perturbations of the state at the reference time, $\boldsymbol{H}$, is full rank. This so-called observability matrix is expressed as

$$\boldsymbol{H} = \frac{\partial \boldsymbol{Y}}{\partial \delta\boldsymbol{x}(t_0)} = \begin{pmatrix} \frac{\partial \boldsymbol{h}}{\partial \delta \boldsymbol{x}}(\boldsymbol{\Phi}(t_0,\tau_1)\delta\boldsymbol{x}(t_0),t_1) \\ \frac{\partial \boldsymbol{h}}{\partial \delta \boldsymbol{x}}(\boldsymbol{\Phi}(t_0,\tau_2)\delta\boldsymbol{x}(t_0),t_2) \\ \vdots \\ \frac{\partial \boldsymbol{h}}{\partial \delta \boldsymbol{x}}(\boldsymbol{\Phi}(t_0,\tau_p)\delta\boldsymbol{x}(t_0),t_p) \end{pmatrix} = \begin{pmatrix} \boldsymbol{C}(\boldsymbol{\Phi}(t_0,\tau_1)\delta\boldsymbol{x}(t_0),t_1)\boldsymbol{\Phi}(t_0,\tau_1) \\ \boldsymbol{C}(\boldsymbol{\Phi}(t_0,\tau_2)\delta\boldsymbol{x}(t_0),t_2)\boldsymbol{\Phi}(t_0,\tau_2) \\ \vdots \\ \boldsymbol{C}(\boldsymbol{\Phi}(t_0,\tau_p)\delta\boldsymbol{x}(t_0),t_p)\boldsymbol{\Phi}(t_0,\tau_p) \end{pmatrix} \tag{32}$$

where sensitivity matrix, $\boldsymbol{C}(\delta\boldsymbol{x}(t),t)$, is the matrix of partial derivatives of the measurements with respect to the state components, given as

$$\boldsymbol{C}(\delta\boldsymbol{x}(t),t) = \left.\frac{\partial \boldsymbol{y}}{\partial \delta \boldsymbol{x}}\right|_{\delta\boldsymbol{x}(t)} \tag{33}$$

Additionally, the qualitative observability of the model depends on the condition number of the observability Gramian, $\boldsymbol{H}^T\boldsymbol{H}$. Large condition numbers indicate a weakly observable system, with 10^{16} suggested as the upper limit for practical observability.[25]

Rectilinear Measurement Sensitivity

To compute the measurement sensitivity with respect to the rectilinear state it is first necessary to compute the sensitivity of the measurement to the relative position in the camera frame. This is given by Gaias[11] as

$$\left.\frac{\partial \boldsymbol{y}}{\partial \boldsymbol{\rho}^c}\right|_{\boldsymbol{\rho}^c} = \frac{1}{||\boldsymbol{\rho}^c||}\begin{bmatrix} -\sin\eta\sin\psi & \cos\psi & -\cos\eta\sin\psi \\ \cos\eta\sec\psi & 0 & -\sin\eta\sec\psi \end{bmatrix} \tag{34}$$

The resulting rectilinear sensitivity matrix, $\boldsymbol{C}_{rect}(\delta\boldsymbol{x}_{rect})$, is computed by using Equation 23 to map the partial derivatives into the RTN frame as

$$\boldsymbol{C}_{rect}(\delta\boldsymbol{x}_{rect}) = \left.\frac{\partial \boldsymbol{y}}{\partial \boldsymbol{\rho}^c}\right|_{\boldsymbol{R}^c_{RTN}\boldsymbol{\rho}} \boldsymbol{R}^c_{RTN} \tag{35}$$

Curvilinear Measurement Sensitivity

The curvilinear measurement sensitivity matrix, $\boldsymbol{C}_{curv}(\delta\boldsymbol{x}_{curv})$, is simply the product of the rectilinear sensitivity matrix evaluated at the position computed using Equation 25 and the partial derivatives of the rectilinear coordinates with respect to the curvilinear coordinates evaluated at the current state as given by

$$\boldsymbol{C}_{curv}(\delta\boldsymbol{x}_{curv}) = \boldsymbol{C}_{rect}(\boldsymbol{\rho}_{rect})\left.\frac{\partial \boldsymbol{\rho}_{rect}}{\partial \delta \boldsymbol{x}_{curv}}\right|_{\delta\boldsymbol{x}_{curv}} \tag{36}$$

and

$$\left.\frac{\partial \boldsymbol{\rho}_{rect}}{\partial \delta \boldsymbol{x}_{curv}}\right|_{\delta\boldsymbol{x}_{curv}} = \begin{bmatrix} c_\theta c_\phi & -\frac{a+\delta r}{a}s_\theta c_\phi & -\frac{a+\delta r}{a}c_\theta s_\phi \\ s_\theta c_\phi & \frac{a+\delta r}{a}c_\theta c_\phi & -\frac{a+\delta r}{a}s_\theta s_\phi \\ s_\phi & 0 & \frac{a+\delta r}{a}c_\phi \end{bmatrix} \tag{37}$$

ROE Measurement Sensitivity

The measurement sensitivity with respect to the ROE state can be computed by applying the chain rule to the sequence of mappings shown in Figure 3 as described in the following.

Linear Map to Rectilinear: The measurement sensitivity is expressed as the product of the rectilinear sensitivity evaluated at $\boldsymbol{T}(t)\delta\boldsymbol{x}_{ROE}$ and the sensitivity of the rectilinear state with respect to the ROE

$$\boldsymbol{C}_{ROE}^{rect}(\delta\boldsymbol{x}_{ROE}) = \boldsymbol{C}_{rect}(\boldsymbol{T}(t)\delta\boldsymbol{x}_{ROE})\boldsymbol{T}(t) \tag{38}$$

Linear Map to Curvilinear: The measurement sensitivity is given by the product of the curvilinear sensitivity evaluated at $\boldsymbol{T}(t)\delta\boldsymbol{x}_{ROE}$ and the sensitivity of the curvilinear state with respect to the ROE

$$\boldsymbol{C}_{ROE}^{curv}(\delta\boldsymbol{x}_{ROE}) = \boldsymbol{C}_{curv}(\boldsymbol{T}(t)\delta\boldsymbol{x}_{ROE})\boldsymbol{T}(t) \tag{39}$$

Nonlinear Map to Rectilinear: Let the nonlinear map from ROE to rectilinear relative position by means of computing the absolute orbits of the spacecraft be denoted by the function $\boldsymbol{g}$. The ROE measurement sensitivity is expressed as the product of the rectilinear sensitivity evaluated at $\boldsymbol{g}(\delta\boldsymbol{x}_{ROE}, t)$ and the sensitivity of the rectilinear state with respect to the ROE

$$\boldsymbol{C}_{ROE}^{nonlin}(\delta\boldsymbol{x}_{ROE}) = \boldsymbol{C}_{rect}(\boldsymbol{g}(\delta\boldsymbol{x}_{ROE}, t))\boldsymbol{T}(t) \tag{40}$$

For J_2-perturbed orbits, each of these sensitivities can instead be evaluated using an osculating ROE state computed via the mean to osculating transformation described by Schaub.[24] It should also be noted that the sensitivity models in Equations 38-40 make the approximation

$$\left.\frac{\partial\delta\boldsymbol{x}_{rect/curv}}{\partial\delta\boldsymbol{x}_{ROE}}\right|_{\delta\boldsymbol{x}_{ROE}(t)} = \left.\frac{\partial\delta\boldsymbol{x}_{rect/curv}}{\partial\delta\boldsymbol{x}_{ROE}}\right|_{\mathbf{0}} = \boldsymbol{T}(t) \tag{41}$$

Numerical Results

The local observability of our proposed dynamic and measurement models is assessed by generating observability matrices for a set of reference trajectories selected to emulate a proximity operations mission. The servicer absolute orbit conditions and the initial mean ROE test cases are given in Table 1. ROE 1 is representative of a far-range hold point. ROE 2 introduces a small relative semi-major axis, allowing the servicer to approach the deputy in a passively safe manner. ROE 3 describes a mid-range hold point. Finally, ROE 4 is a pure along-track separation describing a standard $\boldsymbol{v}$-bar hold point, which is known to be difficult to observe without maneuvers.

Table 1: Initial servicer orbital conditions and mean ROE test cases

Servicer Orbit	$a = 7{,}200$ km	$e = 0.001$	$i = 30°$	$\Omega = 60°$	$\omega = 30°$	$M_0 = 60°$
Initial ROE	$a\delta a\ [m]$	$a\delta\lambda\ [m]$	$a\delta e_x\ [m]$	$a\delta e_y\ [m]$	$a\delta i_x\ [m]$	$a\delta i_y\ [m]$
ROE 1	0	$-30,000$	400	0	-400	0
ROE 2	-150	$-20,000$	300	0	-300	0
ROE 3	0	$-5,000$	0	-200	0	200
ROE 4	0	$-1,000$	0	0	0	0

The performance for each model and is assessed by computing observability matrices for each initial condition described in Table 1 in three test cases. The three cases include propagations of one third of an orbit, one orbit, and ten orbits in order to isolate the effects that can be resolved at sub-orbital, orbital, and multi-orbit time scales. The results presented in the following tables are for cases when measurements are taken in 300 second intervals to simulate a sparse sampling rate. The authors have repeated these tests for sample intervals ranging from 30 seconds to 600 seconds and found that in this range the sample rate has no impact on the rank of the observability matrix and does not change the condition number by more than a factor of ten. This suggests that angles-only navigation system performance should be inherently robust to low sample rates or short data blackouts (e.g. if the camera is temporarily blinded by the sun, or in eclipse). The observability properties of the rectilinear and curvilinear state models in these cases are presented in Table 2. In agreement with previous work,[3] the rectilinear state is never fully observable and always exhibits

Table 2: Observability properties of rectilinear and curvilinear state models

Test Case	Rectilinear state					
	1/3 Orbit		1 Orbit		10 Orbits	
	Rank	Condition	Rank	Condition	Rank	Condition
ROE 1	5	9.806×10^{17}	5	7.724×10^{18}	5	5.329×10^{17}
ROE 2	5	1.091×10^{18}	5	1.684×10^{19}	5	5.322×10^{19}
ROE 3	5	1.490×10^{18}	5	1.409×10^{19}	5	1.874×10^{19}
ROE 4	5	2.485×10^{18}	5	4.774×10^{20}	5	3.291×10^{21}
	Curvilinear state					
	Rank	Condition	Rank	Condition	Rank	Condition
ROE 1	6	2.532×10^{17}	6	1.177×10^{15}	6	7.892×10^{12}
ROE 2	6	1.215×10^{18}	6	6.416×10^{14}	6	2.252×10^{14}
ROE 3	6	4.189×10^{16}	6	4.538×10^{15}	6	3.752×10^{14}
ROE 4	6	5.118×10^{17}	6	4.620×10^{22}	6	3.247×10^{20}

very large condition numbers. The curvilinear state is instead able to achieve full rank, but the condition numbers for this model are still very poor.

Next, the observability properties of the ROE state models under the assumption of a Keplerian orbit are shown in Table 3. The measurement model that linearly maps the ROE state to rectilinear position (Figure 3, $\boldsymbol{y}_1$) is never fully observablee, in agreement with Gaias.[11] Additionally, use of the nonlinear map between ROE and relative position in $\boldsymbol{y}_2$ and $\boldsymbol{y}_3$ achieves full observability for all trajectories without considering J_2 effects, in agreement with Lovell and Lee.[6] It is noteworthy that use of the linear map to curvilinear coordinates ($\boldsymbol{y}_2$) recovers full rank in the observability matrix with similar condition numbers to the nonlinear map ($\boldsymbol{y}_3$) in all cases.

Finally, the condition number of the observability matrices for models including J_2 effects and the nonlinear map from ROE to rectilinear position are shown in Table 4. The rank of the condition matrix is excluded for brevity as all of the included models are fully observable. Also, the condition numbers of the linear maps to rectilinear and curvilinear states are not included, but exhibit similar properties. Eccentricity effects are assessed in these tests by comparing the condition number of models including the full STM from Equation 20 (top) and the simplified STM from Equation 21 (bottom). Similarly, periodic effects are assessed by comparing the condition numbers of models with (right) and without (left) the mean to osculating transformation. By comparing the condition number of the models in Table 3 with those on the left side of Table 4, it is evident that inclusion of J_2 effects in the STM provides only a small improvement to system observability. Additionally, the difference in condition number between the full and simplified J_2 STMs is negligible. It follows that use of the simplified STM for near-circular orbits is justified in order to save computational effort. The most significant improvement in condition number is achieved by including the mean to osculating transformation in the measurement model as long as the propagation time is at least one orbit. The condition numbers for these models are several orders of magnitude smaller than those published by other authors.[6,7,11] This result suggests that inclusion of this transformation is essential to resolving the range ambiguity in maneuver-free angles-only navigation. Furthermore, future study of this transformation may provide geometric insight that can be modeled at low computational cost.

INITIAL RELATIVE ORBIT DETERMINATION USING SCALED ROE

Since only bearing angle measurements are available, a complete state estimation architecture will require an Initial Relative Orbit Determination (IROD) which provides a reasonable a-priori initialization to the sequential estimation filter at minimal computational burden. In the framework of orbital rendezvous, research by Bingham proposes using the Gauss initial orbit determination method combined with an iterative refine-

Table 3: Observability properties of ROE measurement models for Keplerian orbits

Test Case	$\boldsymbol{y}_1$ Model: Linear map to rectilinear relative position					
	1/3 Orbit		1 Orbit		10 Orbits	
	Rank	Condition	Rank	Condition	Rank	Condition
ROE 1	5	2.056×10^{18}	5	1.241×10^{16}	5	4.525×10^{16}
ROE 2	5	9.848×10^{16}	5	5.883×10^{17}	5	4.382×10^{17}
ROE 3	5	7.931×10^{16}	5	3.218×10^{16}	5	1.003×10^{17}
ROE 4	5	8.458×10^{16}	5	1.954×10^{17}	5	5.365×10^{17}
	$\boldsymbol{y}_2$ Model: Linear map to curvilinear position					
Test Case	1/3 Orbit		1 Orbit		10 Orbits	
	Rank	Condition	Rank	Condition	Rank	Condition
ROE 1	6	1.314×10^{10}	6	2.254×10^{8}	6	2.624×10^{6}
ROE 2	6	2.236×10^{10}	6	2.086×10^{8}	6	7.879×10^{7}
ROE 3	6	6.274×10^{10}	6	7.523×10^{8}	6	9.324×10^{7}
ROE 4	6	1.015×10^{17}	6	1.209×10^{16}	6	5.748×10^{13}
	$\boldsymbol{y}_3$ Model: Nonlinear map to relative position					
Test Case	1/3 Orbit		1 Orbit		10 Orbits	
	Rank	Condition	Rank	Condition	Rank	Condition
ROE 1	6	1.261×10^{10}	6	2.414×10^{8}	6	4.542×10^{6}
ROE 2	6	2.163×10^{10}	6	1.907×10^{8}	6	8.168×10^{7}
ROE 3	6	7.506×10^{10}	6	7.791×10^{8}	6	9.730×10^{7}
ROE 4	6	1.214×10^{17}	6	1.137×10^{16}	6	5.897×10^{13}

Table 4: Observability of ROE models of J_2-perturbed orbits

	$\boldsymbol{y}_3$ measurement model, full J_2			$\boldsymbol{y}_6$ measurement model, full J_2		
Initial ROE	1/3 Orbit	1 Orbit	10 Orbits	1/3 Orbit	1 Orbit	10 Orbits
ROE 1	7.145×10^{9}	3.017×10^{8}	4.632×10^{6}	8.670×10^{9}	2.345×10^{3}	1.450×10^{3}
ROE 2	9.337×10^{9}	1.647×10^{8}	8.304×10^{7}	1.476×10^{10}	4.358×10^{2}	1.255×10^{3}
ROE 3	3.101×10^{10}	2.286×10^{8}	8.580×10^{7}	2.752×10^{10}	2.025×10^{3}	1.405×10^{3}
ROE 4	6.982×10^{13}	9.532×10^{11}	1.763×10^{11}	5.242×10^{10}	5.519×10^{4}	6.197×10^{3}
	$\boldsymbol{y}_3$ measurement model, simple J_2			$\boldsymbol{y}_6$ measurement model, simple J_2		
Initial ROE	1/3 Orbit	1 Orbit	10 Orbits	1/3 Orbit	1 Orbit	10 Orbits
ROE 1	7.144×10^{9}	3.017×10^{8}	4.631×10^{6}	8.670×10^{9}	2.345×10^{3}	1.450×10^{3}
ROE 2	9.337×10^{9}	1.647×10^{8}	8.305×10^{7}	1.476×10^{10}	4.358×10^{2}	1.255×10^{3}
ROE 3	3.101×10^{10}	2.286×10^{8}	8.580×10^{7}	2.752×10^{10}	2.025×10^{3}	1.405×10^{3}
ROE 4	6.974×10^{13}	9.528×10^{11}	1.767×10^{11}	5.242×10^{10}	5.519×10^{4}	6.197×10^{3}

ment of the solution via nonlinear least squares.[26] However, this approach is shown to be markedly sensitive to the bearing angle measurement errors. Karimi has posed a solution to reduce the noise sensitivity by performing curve-fitting of the measured line-of-sight vectors, however the subsequent space-based relative orbit determination requires iterative gradient descent computation to produce the final estimate.[27] Instead, the procedure used during the ARGON phase of PRISMA relied on coarse state initialization via two-line elements (TLEs) provided by NORAD and propagated using the Simplified General Perturbation Model 4 (SGP4).[21] Applying a batch least-squares filter to improve the propagated data, the researchers concluded

that the strategy provided enough accuracy to initiate a safe along-track separation of the two spacecraft but not enough accuracy to establish a reliable relative eccentricity/inclination-vector separation.

Based on the limitations discovered during the ARGON experiment, we propose a simpler approach to IROD which uses a batch of bearing angle measurements and only relies on TLE for initializing the mean along-track separation. In this context, it will be shown that a scaling of the ROE state in Equation 5 by the mean along-track separation, $\delta\lambda$, produces a modified scaled ROE (SROE) state that is strongly observable irrespective of the uncertainty in along-track position. Accordingly, the SROE state can be solved for directly from the measurement set using a batch least-squares approach and used in conjunction with an estimate of $\delta\lambda$ for initialization of the complete sequential estimation algorithm. Consider the SROE state

$$\delta\hat{\boldsymbol{x}}_{ROE} = \frac{1}{\delta\lambda}\begin{pmatrix}\delta a & \delta e_x & \delta e_y & \delta i_x & \delta i_y\end{pmatrix}^T = \begin{pmatrix}\delta\hat{a} & \delta\hat{e}_x & \delta\hat{e}_y & \delta\hat{i}_x & \delta\hat{i}_y\end{pmatrix}^T \tag{42}$$

subject to Keplerian unperturbed dynamics. Following from Equation 7, the equations of motion for this modified state become nonlinear in the form

$$\delta\dot{\hat{\boldsymbol{x}}}_{ROE} = 1.5n\delta\hat{a}\delta\hat{\boldsymbol{x}}_{ROE} \tag{43}$$

For practical purposes, it is reasonable to assume a nonzero mean along-track separation that is much larger than the other five unscaled parameters (e.g. $\delta\lambda >> \delta a$, etc.) and that the time-step between measurements is small with respect to the orbital period. In this context, the time evolution of the SROE elements over the propagation time is effectively zero and the STM is identity.

Linearized Measurement Model for Scaled ROE

The relationship between the ROE and the relative position according to the HCW equations lends itself to a simple linear measurement model for the SROE state. Consider Equation 26 normalized by $a\delta\lambda$ and mapped by Equation 23 to the following camera frame scaled positions

$$\frac{\rho_x^c}{a\delta\lambda} = \delta\hat{a} - \delta\hat{e}_x c_u - \delta\hat{e}_y s_u \qquad \frac{\rho_y^c}{a\delta\lambda} = -\delta\hat{i}_x s_u + \delta\hat{i}_y c_u \qquad \frac{\rho_z^c}{a\delta\lambda} = -1 - 2\delta\hat{e}_y c_u + 2\delta\hat{e}_x s_u \tag{44}$$

The HCW assumptions of small relative motion are not generally satisfied in the angles-only navigation problem where large mean along-track separations are common. In that case, observed offsets in the radial motion are caused by a combination of the relative semi-major axis and orbit curvature effects due to a nonzero mean along-track separation. For near-circular orbits with no relative semi-major axis, the servicer, target, and center of the earth form an isosceles triangle as shown in Figure 5. From this geometry, it is evident

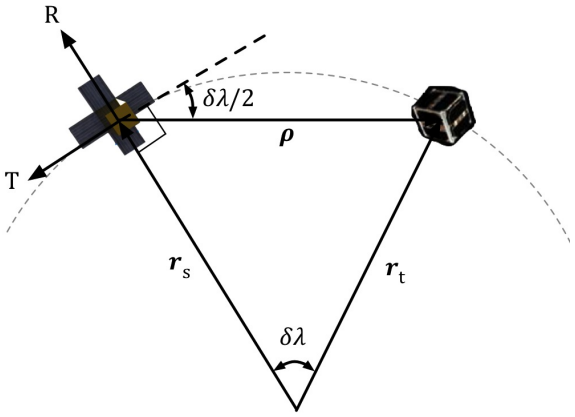

Figure 5: Radial offset caused by mean along-track separation and orbit curvature.

that the scaled radial offset observed due to the along-track separation is $-|\delta\lambda|/2$. Thus, the corrected scaled radial position is expressed as

$$\frac{\rho_x^c}{a\delta\lambda} = \delta\hat{a} - \delta\hat{e}_x c_u - \delta\hat{e}_y s_u - |\delta\lambda|/2 \tag{45}$$

Substituting Equations 44 and 45 into Equation 24 and linearizing about $\delta\hat{\boldsymbol{x}}_{_{ROE}} = \mathbf{0}$ yields

$$\sin\eta = -\delta\hat{i}_x s_u + \delta\hat{i}_y c_u \qquad \tan\psi = \delta\hat{a} - \delta\hat{e}_x c_u - \delta\hat{e}_y s_u - |\delta\lambda|/2 \tag{46}$$

Separating the a-priori estimate of $\delta\lambda$ results in the measurement equation

$$\boldsymbol{y}(t) = \begin{pmatrix} \sin\eta \\ \tan\psi + \frac{|\delta\lambda|}{2} \end{pmatrix} = \begin{bmatrix} 0 & 0 & 0 & -s_u & c_u \\ 1 & -c_u & -s_u & 0 & 0 \end{bmatrix} \delta\hat{\boldsymbol{x}}_{_{ROE}} = \hat{\boldsymbol{C}}_{_{ROE}}(t)\delta\hat{\boldsymbol{x}}_{_{ROE}} \tag{47}$$

The complete measurement vector, $\boldsymbol{Y}$, is composed of the $\boldsymbol{y}$ vectors from all measurement times.

Scaled ROE Observability

Since the SROE time-evolution is stationary, the observability matrix, $\mathbf{H}$, is built simply by concatenating the measurement matrices, $\hat{\boldsymbol{C}}_{_{ROE}}(t)$, at each measurement epoch. A minimum of three sets of azimuth and elevation angles is required to reconstruct the five SROE. If $\boldsymbol{H}^T\boldsymbol{H}$ is nonsingular and thus invertible, the system is observable and the SROE can be computed directly from the set of measurements. Denoting the servicer mean argument of latitude at the three measurement epochs as u_1, u_2, and u_3, the determinant of the observability Gramian is expressed as

$$|\boldsymbol{H}^T\boldsymbol{H}| = -\frac{1}{2}\left(c_{2(u_1-u_2)} + c_{2(u_1-u_3)} + c_{2(u_2-u_3)} - 3\right)\left(s_{u_1-u_2} - s_{u_1-u_3} + s_{u_2-u_3}\right)^2 \tag{48}$$

Clearly, the determinant of the observability Gramian is zero only when $u_1 = u_2 = u_3$. Furthermore, the determinant is very small when $u_1 \approx u_2 \approx u_3$. Therefore, for good condition number, the measurement epochs should be sufficiently separated. A sequence of equally spaced measurements over the course of an orbit is sufficient to satisfy this requirement.

Weighted Least-Squares Solution: Let us assume that there are p distinct measurement intervals satisfying the observability conditions above. This provides $2p$ measurements that are related to the five unknown scaled ROE via the observability matrix

$$\boldsymbol{Y} = \boldsymbol{H}\delta\hat{\boldsymbol{x}}_{_{ROE}} \qquad \boldsymbol{Y} \in \mathbb{R}^{2\mathrm{p}\times 1} \quad \boldsymbol{H} \in \mathbb{R}^{2\mathrm{p}\times 5} \tag{49}$$

Furthermore, the azimuth and elevation angles are assumed to be uncorrelated Guassian random variables with known variances, σ_η^2 and σ_ψ^2. For $p \geq 3$, this is an overdetermined system of linear equations for which a least-squares solution exists in the form

$$\delta\hat{\boldsymbol{x}}_{_{ROE}}^{^{L.S}} = \left(\boldsymbol{H}^{^T}\boldsymbol{W}\boldsymbol{H}\right)^{-1}\boldsymbol{H}^{^T}\boldsymbol{W}\boldsymbol{Y} \qquad \boldsymbol{W} \in \mathbb{R}^{2\mathrm{p}\times 2\mathrm{p}} \tag{50}$$

The weight matrix, $\boldsymbol{W}$, is the inverse of the combined measurement covariance matrix. Since the observability Gramian is nonsingular, a unique least-squares solution is guaranteed to exist. The covariance matrix of the least-squares solution is

$$\mathrm{Cov}\left[\delta\hat{\boldsymbol{x}}_{_{ROE}}^{^{L.S}}\right] = \left(\boldsymbol{H}^{^T}\boldsymbol{W}\boldsymbol{H}\right)^{-1} \tag{51}$$

Filter Initialization

Although it has been shown that the SROE state can be estimated directly from a set of azimuth and elevation angle measurements, an estimate of the mean along-track separation, $a\delta\lambda$, is still required to complete the navigation filter initialization. For this paper, a simple procedure is used to convert the SROE to mean ROE which relies on coarse mean along-track separation knowledge that can be generally obtained from a NORAD TLE set. However, unlike the approach used for the ARGON experiment,[21] the use of TLEs in this context is confined to directly estimating $a\delta\lambda$ only. The initial mean ROE estimate is computed by multiplying the estimated SROE by the provided $a\delta\lambda$. The initial mean ROE variances are estimated from the scaled ROE variances from Equation 51 combined with the variance of the estimated mean along-track separation, $\sigma_{\delta\lambda}^2$. The variance of the initial mean ROE element corresponding to the j^{th} SROE element, $\delta\hat{x}_{j,_{ROE}}$, is

$$\sigma_{\delta x_{j,_{ROE}}}^2 = \delta\hat{x}_{j,_{ROE}}^2\delta\lambda^2\left[\left(\frac{\sigma_{\delta\hat{x}_{j,_{ROE}}}}{\delta\hat{x}_{j,_{ROE}}}\right)^2 + \left(\frac{\sigma_{\delta\lambda}}{\delta\lambda}\right)^2\right] \tag{52}$$

HIGH-FIDELITY VALIDATION

The previous observability analysis established that inclusion of nonlinearities in the measurement model grants full local observability to the angles-only navigation problem. However, the condition number of the observability Gramian depends strongly on which nonlinear effects are modeled. Specifically, inclusion of the mean to osculating transformation provides a significant improvement in the condition number of the observability Gramian compared to those provided in literature if data for at least a full orbit is available. However, local observability of the model is a necessary but not sufficient condition to validate its suitability for a maneuver-free angles only navigation filter. It is still possible that errors in the modeled measurements may prevent the filter from converging on the true range. With this in mind, the proposed IROD algorithm and previously described dynamic and measurement models are further evaluated through implementation in high-fidelity simulations of a complete maneuver-free angles only navigation system subject to the constraints of realistic guidance, navigation, and control systems.

In each simulation, the orbits of the servicer and target are initialized with one of the initial conditions specified in Table 1. The position and velocity of each spacecraft are numerically propagated for ten orbits using rigorous force models including GRACE's GGM01S geopotential model of order and degree 120,[28] a cannonball model for atmospheric drag,[29] analytical models for third-body gravity from the sun and moon,[30] and solar radiation pressure including a conical earth shadow model. From the simulated trajectories, sets of GPS measurements of the servicer orbit and bearing angle measurements between the spacecraft are generated including realistic noise models from current commercial off-the-shelf sensors.[31–33] Key parameters of the noise models are summarized in Table 5.

Table 5: Simulation noise nources

Bearing Angles	Servicer Knowledge			
$\sigma_{\eta,\psi}$[31]	Off-Axis Attitude[32]	Roll-Axis Attitude[32]	GPS Position[33]	GPS Velocity[33]
40”	6”	40”	10 m	0.1 m/s

IROD Validation

The performance of the IROD algorithm is assessed by comparing the estimated SROE using the previously described simulated measurements to the SROE from the simulation environment. Specifically, the ground truth SROE are computed by applying Equation 42 to the true mean ROE at the time of the final measurement when the initialization is performed. These true mean ROE are computed by applying the osculating to mean transformation described by Schaub[24] to the corresponding osculating ROE from the simulation environment. This assessment is performed for all of the initial states described in Table 1 including errors in the a-priori estimate of $\delta\lambda$ ranging from 0% to 25% of the true value. Additionally, the initialization is performed with two different data sets to determine the effect of propagation time. The first data set consists of seven pairs of bearing angles each separated by 300 seconds for a total elapsed time of one third of an orbit. The second data set consists of 21 sets of angles for a total propagation time of one orbit. The estimation errors from this assessment are shown in Figure 6.

Several conclusions can be drawn from these results. First, it is clear that the estimation error does not depend on the $\delta\lambda$ initialization error. Additional testing also shows that the estimation error is largely uninfluenced by the measurement noise. These two conclusions are a strong indication that the main source of error in the estimation comes from the neglected dynamics and simplified measurement model. All SROE errors are less than 0.002, and often less than 0.001 with one notable exception being the ROE 3 case for the small measurement set. This is because the true values of the SROE in this case ($\sim$0.05) are significantly larger than in all other cases. Accordingly, the linear measurement model is not as valid nor as accurate. Interestingly, this error vanishes when initialization is performed using the large data set. This behavior can be understood by considering the geometry illustrated in Figure 4. The relative eccentricity vector produces an oscillation in the along track separation, resulting in a warping of the azimuth and elevation angles. Because the small data set only includes one third of an orbit, the algorithm is unable to accurately resolve the shape

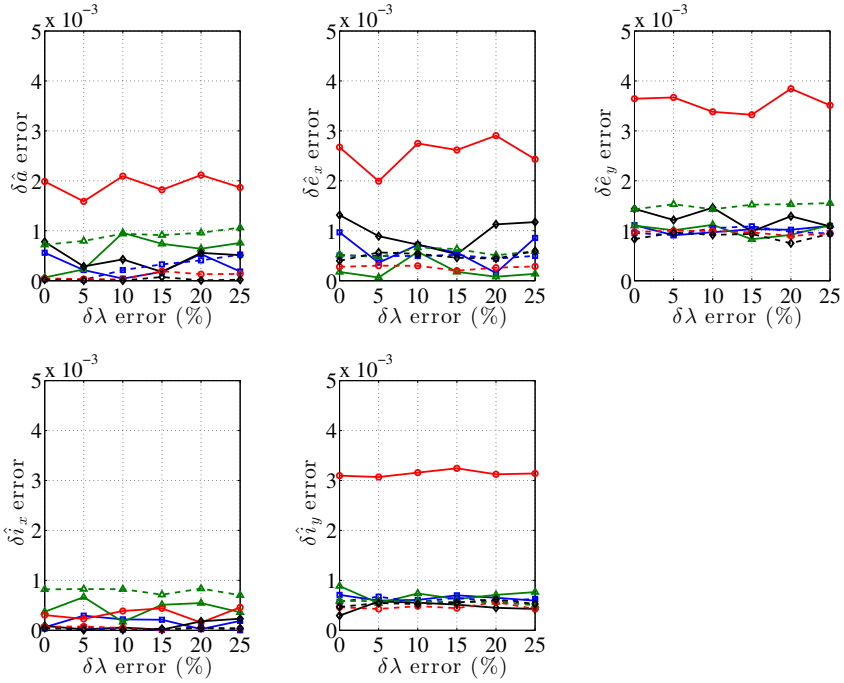

Figure 6: Estimation error of SROE vs error of a-priori $\delta\lambda$ estimate over small (solid) and large (dashed) propagation times for ROE 1 (blue), ROE 2 (green), ROE 3 (red), ROE 4 (black) cases.

of this warping. However, when an entire orbit of data is considered, the warping effect is averaged out, resulting in improved estimation accuracy. Additionally, consider the magnitude of the resulting estimation error for the large measurement set. At a mean along-track separation of 20 km, an error of 0.002 in any of the SROE maps to an error of 40 meters in the corresponding ROE. Considering that the true unscaled ROE values are on the order of a few hundred meters, these errors are not negligible. Accordingly, study of potential improvements of this method including incorporation of nonlinearities in the dynamic and measurement models is necessary.

Navigation System Model Validation

The full navigation system concept is validated through high-fidelity simulations of state initialization using the described IROD algorithm and subsequent state estimation using a sequential extended Kalman filter (EKF). In order to maximize initialization accuracy, the IROD algorithm is executed with 21 sets of bearing angle measurements, corresponding to one complete orbit. The a-priori estimate of $a\delta\lambda$ fed into the algorithm includes an error and corresponding uncertainty of 10% of the true value, which is comparable to the accuracy of range estimates from TLEs at large separations.[21] The initial ROE covariance estimate is computed assuming uncorrelated errors from the initial SROE estimate and uncertainty using Equation 52.

The initial state estimate is propagated with EKFs incorporating the rectilinear, curvilinear, and mean ROE states. The filters perform a measurement update every 300 seconds and assume a 60 arcsecond 1-σ measurement noise to account for the cumulative noise from sources described in Table 5. The filters using the ROE state assume a uniform uncorrelated 1-σ process noise of 6 m in each of the ROE components. In light of the results of the observability analysis, all of these filters employ the simplified J_2 STM for near-circular orbits in the dynamic model. Additionally, all six of the previously described measurement models are included.

The initial rectilinear state estimate is computed from the absolute orbits of both spacecraft, which are calculated from the servicer GPS measurements and initial ROE from the IROD algorithm. The initial curvi-

linear state estimate is subsequently computed from the rectilinear estimate. The initial covariance of these state estimates, $\boldsymbol{P}_{rect/curv}$, is computed from the initial ROE covariance, $\boldsymbol{P}_{ROE}$, using the law of linear covariance propagation

$$\boldsymbol{P}_{rect/curv} = \boldsymbol{T}(t)\boldsymbol{P}_{ROE}\boldsymbol{T}(t)^T \tag{53}$$

The process noise for the rectilinear and curvilinear states is similarly computed from the ROE process noise using Equation 53.

First, consider the behavior of the estimation error of the curvilinear (left) and rectilinear (right) state filters as shown in Figure 7 for the trajectory evolving from initial condition ROE 2. It is evident that the

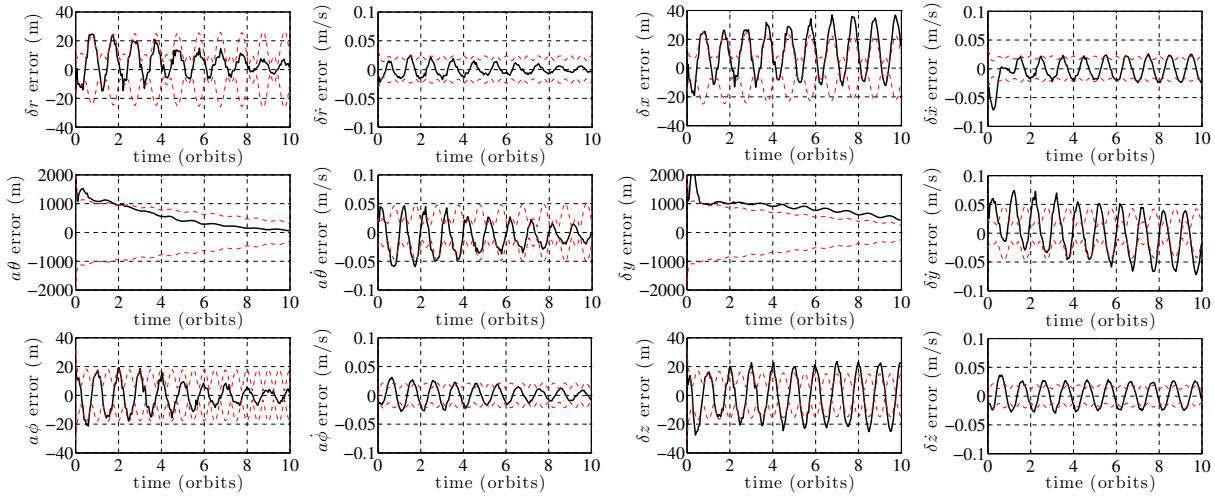

Figure 7: Evolution of state estimation error (black) and 1-σ covariance bounds (red, dotted) for EKFs using curvilinear (left) and rectilinear (right) state models for ROE 2 trajectory

curvilinear filter is able to slowly converge on the true along-track separation. It is noteworthy that the other state elements exhibit oscillations at the same period as the orbit which decay with the along-track error. Furthermore, the oscillation in the along-track velocity error has twice the amplitude and is out of phase with the radial velocity error. This behavior is characteristic of the HCW equations (Equation 26) and therefore supports the intuition that the shape and orientation of the relative motion are observable, but the state estimates are scaled by the along-track separation. On the other hand, the rectilinear state is unable to converge on the along-track separation and exhibits persistent error oscillations throughout the simulation. This is expected since the previous observability analysis and studies by previous authors have demonstrated that fully linear models of the relative position are not fully observable.

The filters using the mean ROE state show significantly improved performance. Figure 8 provides the evolution of the estimation error for filters using the six ROE state measurement models following trajectory ROE 2. For comparison with the ground truth, the output of the filter is mapped into osculating ROE space using the previously described mean to osculating transformation. These plots have several noteworthy features. First, the estimation errors for these filters do not exhibit the oscillations characteristic of the rectilinear and curvilinear state filters. Second, as expected, the filters incorporating the $\boldsymbol{y}_1$ and $\boldsymbol{y}_4$ measurement models (using the linear map to rectilinear position) are not able to converge to the true relative mean longitude, and accordingly exhibit substantial biases in estimates of the other ROE. Third, the filters incorporating the $\boldsymbol{y}_2$ and $\boldsymbol{y}_5$ measurement models (using the linear map to curvilinear position) are able to converge to the true value of $a\delta\lambda$ at a similar rate to the curvilinear state filter. However, errors in the relative position modeling result in residual biases of approximately ten meters in relative eccentricity. The filters including the $\boldsymbol{y}_3$ and $\boldsymbol{y}_6$ measurement models (using the nonlinear map to rectilinear position) are able to reduce the error in $a\delta\lambda$ to a few hundreds of meters in only a few orbits and show no significant residual biases in $a\delta a$ or $a\delta\boldsymbol{e}$. It is also interesting to note that the average estimates of $a\delta\lambda$, $a\delta e_x$, and $a\delta i_x$ converge at the same rate, while

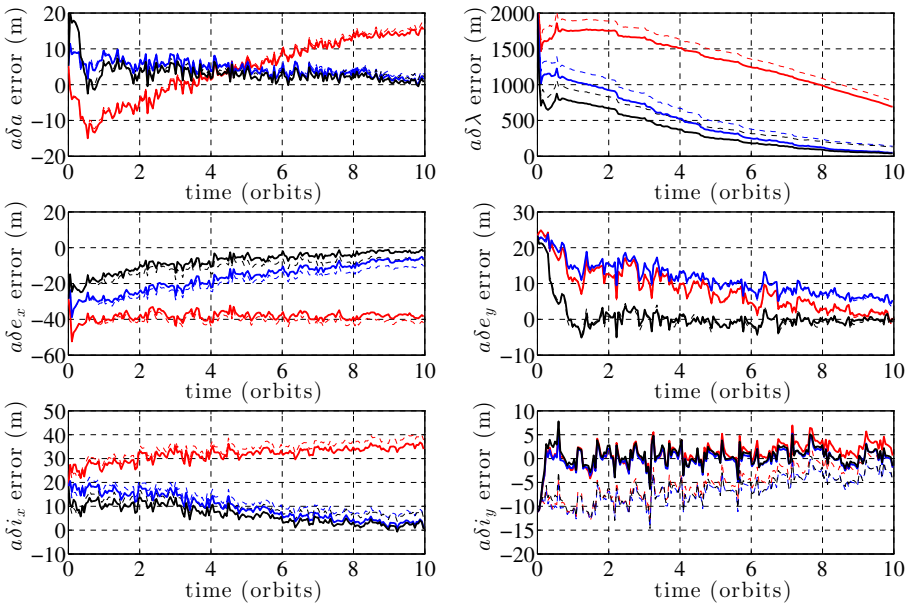

Figure 8: Evolution of osculating ROE estimation error for rectilinear (red, thin), curvilinear (blue, medium), and nonlinear (black, thick) relative position maps with (solid) and without (dotted) the mean to osculating transformation in the measurement model for ROE 2 trajectory

the average estimates of $a\delta e_y$, and $a\delta i_y$ converge within one orbit. Recalling that $a\delta e_y$ and $a\delta i_y$ are zero for ROE 2, these results support the interpretation that the shape is observable, but the state estimates scale with $a\delta\lambda$. As a final note, inclusion of the mean to osculating transformation removes a 10 meter bias in δi_y for all measurement models. This suggests that there is a consistent geometric effect embedded in this transformation that can be leveraged to improve the performance of simpler measurement models. This is also consistent with our previous analysis suggesting that inclusion of this transformation improves observability of the relative motion.

In the interest of rigor, it is necessary to directly compare the performance of the mean ROE and translational state filters. Figure 9 presents a comparison of the estimation error of the best-performing ROE filter (using the $\boldsymbol{y}_6$ measurement model) with the curvilinear state filter (mapped into osculating ROE space) including 1-σ uncertainty bounds for the ROE 2 trajectory. It is clear that the behavior of the curvilinear state estimation error is similar to that of the ROE filters incorporating the $\boldsymbol{y}_2$ measurement model (indicated by a dashed blue line in Figure 8). Specifically, it exhibits a slow convergence on the true relative mean longitude and persistent biases of approximately ten meters in relative eccentricity and inclination. However, the curvilinear state filter also exhibits oscillations of tens of meters in all of the state estimates. The mean ROE state filter with the $\boldsymbol{y}_6$ measurement model exhibits clearly superior performance including more rapid convergence on the true relative mean longitude, no residual biases in any of the ROE, and immunity to the oscillations of the state estimates.

It is also interesting to consider the relationship between the initial state and filter performance. Table 6 presents a comparison of the initialization error with the average and standard deviation of the final estimation error produced by the EKF. The final values are computed from the error profile of the last complete orbit of the simulation. It is clear that the filter is able to substantially reduce the $a\delta\lambda$ error for initial conditions ROE 1 and ROE 2, but provides little benefit for initial conditions ROE 3 and ROE 4. As demonstrated in the previous observability analysis, inclusion of nonlinearities in the measurement model is key to resolving the range ambiguity. At small separations, such as ROE 3 and ROE 4, the filter may be unable to resolve the nonlinear effects in the presence of measurement noise.

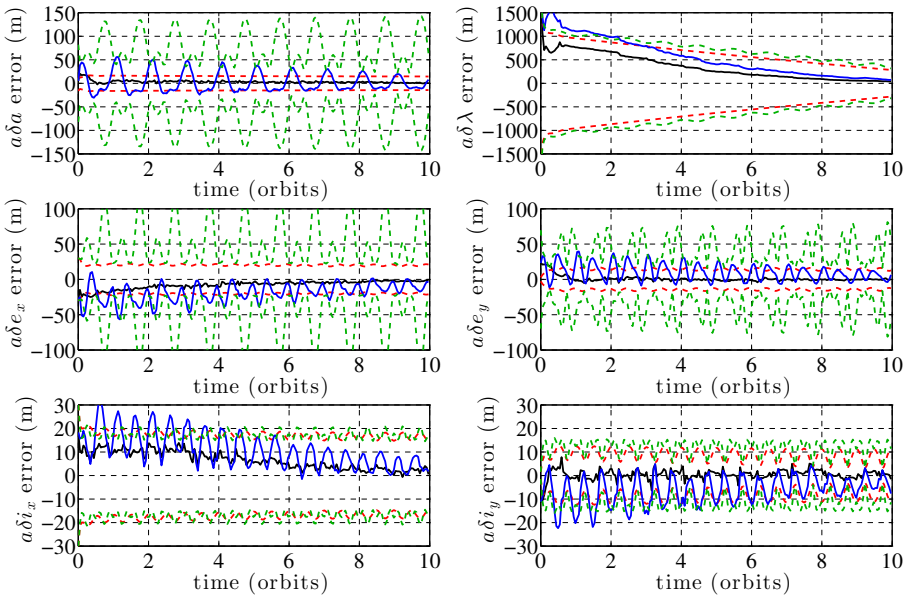

Figure 9: Comparison of estimation error for EKFs using mean ROE (black) and curvilinear (blue) states in osculating ROE space. The ROE filter includes the mean to osculating transformation and nonlinear map to relative position in the measurement model. Associated 1-σ bounds for ROE (red, dotted) and curvilinear (green, dotted) filters are shown.

Overall, the ROE state filter using the $\boldsymbol{y}_6$ measurement model is able to bound the error in relative mean longitude to less than one kilometer and the error in the remaining ROE to a few tens of meters for all tested initial states. This is sufficient to ensure passively safe relative motion through relative eccentricity/inclination-vector separation. Furthermore, without requiring use of maneuvers, the filter is able to achieve estimation errors comparable to results published by other authors using approaches requiring impulsive maneuvers.[11] It is also noteworthy that simpler measurement models ($\boldsymbol{y}_2$, $\boldsymbol{y}_3$, and $\boldsymbol{y}_5$) also converge on the true along-track separation. It follows that such simple models may be suitable for mission applications with less demanding navigation accuracy requirements. Additionally, these results confirm the intuition from the observability analysis that capturing the nonlinearities in the evolution of the relative motion improves navigation performance, suggesting that implementation of a maneuver-free angles-only navigation system is feasible. However, the authors have noticed that the filter exhibits strong sensitivity to initialization errors and filter noise parameters, which will be addressed in future work.

CONCLUSIONS

This work presented the design and validation of a novel angles-only relative navigation architecture. Whereas the majority of previous approaches utilize maneuvers to rectify the well-documented range observability issues, this design demonstrates comparable navigation capability in a variety of scenarios without prompting orbit or attitude maneuvers. First, a comparison of the dynamic models of relative motion was conducted considering the rectilinear, curvilinear, and relative orbital element state representations. Within the framework of the ROE state, a new model for J_2-perturbed relative motion in orbits of arbitrary eccentricity is developed using Floquet theory. In addition to this elegant inclusion of perturbations, the ROE model provides illuminating geometrical insight into the relative motion and conveniently decouples the unobservable range from the remaining state elements. A rigorous improvement of the angles-only measurement sensitivity models was achieved by preserving nonlinearities in the transformation of the curvilinear and ROE states to modeled bearing measurements in the camera frame. The combined improvements to the dynamics and measurement models were quantified in a comprehensive observability assessment. The results strongly

Table 6: Comparison of initialization error (ϵ_i) with the average final estimation error (ϵ_f) and standard deviations (σ_f) for ROE state filter using $\boldsymbol{y}_6$ measurement model for each initial condition. The final values are computed from the estimation error profile over one orbit.

	ROE 1			ROE 2			ROE 3			ROE 4		
	ϵ_i	ϵ_f	σ_f	ϵ_i	ϵ_f	σ_f	ϵ_i	ϵ_f	σ_f	ϵ_i	ϵ_f	σ_f
$a\delta a$ (m)	6.0	0.24	14	2.4	1.4	6.2	0.62	0.32	2.5	0.02	0.04	0.47
$a\delta\lambda$ (km)	3.0	0.21	0.72	2.0	0.07	0.24	0.50	0.45	0.01	0.10	0.09	0.01
$a\delta e_x$ (m)	54	3.2	21	25	-4.5	10	1.1	0.10	3.8	0.47	0.01	0.78
$a\delta e_y$ (m)	26	0.91	19	25	-0.69	8.6	24	17	3.4	0.73	0.03	0.54
$a\delta i_x$ (m)	36	5.7	13	21	3.1	5.8	0.30	-0.10	2.4	0.01	-0.05	0.41
$a\delta i_y$ (m)	14	-1.5	12	10	-0.49	5.9	22	18	2.1	0.47	-0.05	0.43

indicate that observability is greatly improved by capturing the nonlinearities in the measurement models. In particular, the model that includes both the transformation from mean to osculating ROE and the nonlinear map from osculating ROE to rectilinear position demonstrates condition numbers that are several orders of magnitude smaller than those available in literature.

The insight gained from the state comparison and observability assessment informed the design of a series of navigation filters created to test the capabilities of each relevant dynamic/measurement model combination. An initial relative orbit determination method was developed which leverages the ROE decoupling of the unobservable range to provide improved initialization to the filters. In several of the test cases, the filters which include nonlinearities in the measurement sensitivity formulations are able to constrain the estimation error to tolerable values on the order of tens of meters and reduce the initial range error by an order of magnitude within a few orbits when tested in high-fidelity. In the context of mid- to far-range navigation and rendezvous, this estimation error is sufficient to establish passively safe relative motion through an eccentricity/inclination-vector separation. Finally, this performance was demonstrated to be superior to models using translational state representations with the Hill-Clohessy-Wiltshire equations. In particular, the ROE state filter exhibits no residual biases in the state estimates and immunity to the error oscillations characterizing the translational state filters.

The results of this work suggest potential research avenues for further study. As indicated during the algorithm validation, the navigation filters demonstrate strong sensitivity to the initialization error. Thus, future iterations should improve upon the proposed initial relative orbit determination approach by considering the full nonlinear dynamics in order to limit dependence on unreliable TLE data. Second, it will be necessary to better understand the geometric implications of the mean to osculating transformation used in the measurement modeling. It is hoped that this study will reveal patterns that can be included in the measurement model at low computational cost. Finally, while the near-circular assumption was enacted for relevance to the proposed mSTAR mission, the improved J_2-perturbed STM holds for orbits of arbitrary eccentricity. Generalizing the measurement models to eccentric orbits and aiming to reduce overall computational burden will pave the way for extending this work to many mission applications.

Overall, this work presents conclusive evidence that improvements to the dynamic and measurement models make maneuver-free angles-only navigation feasible. Implementation of the proposed algorithms in designated vision-based navigation and rendezvous architectures has the potential to reduce operational costs of proximity operations, thereby increasing the capabilities of future distributed space system missions.

ACKNOWLEDGEMENTS

This work was partially supported by a NASA Office of the Chief Technologists Space Technology Research Fellowship (NSTRF), NASA Grant #NNX15AP70H.

REFERENCES

[1] S. D'Amico, M. Pavone, S. Saraf, A. Alhussien, T. Al-Saud, S. Buchman, R. Bryer, and C. Farhat, "Miniaturized Autonomous Distributed Space Systems for Future Science and Exploration," *8th IWSCFF*, Delft University, 2015.

[2] A. Koenig, S. D'Amico, B. Macintosh, and C. Titus, "Formation Design Analysis for a Miniaturized Distributed Occulter/Telescope in Earth Orbit," *International Symposium on Space Flight Dynamics (ISSFD)*, 2015.

[3] D. Woffinden and D. Geller, "Observability Criteria for Angles-Only Navigation," *IEEE Transactions on Aerospace and Electronic Systems*, Vol. 45, No. 3, 2009, pp. 1194–1208.

[4] D. Woffinden and D. Geller, "Optimal Orbital Rendezvous Maneuvering for Angles-Only Navigation," *Journal of Guidance, Control, and Dynamics*, Vol. 32, No. 4, 2009, pp. 1382–1387.

[5] R. Christensen and D. Geller, "Spin-Assisted Angles-Only Navigation and Control for Smallsats," *AAS Guidance and Control Conference*, 2014.

[6] T. A. Lovell and T. Lee, "Nonlinear Observability for Relative Satellite Orbits with Angles-Only Measurements," *International Symposium on Space Flight Dynamics (ISSFD)*, 2014.

[7] J. Wang, E. Butcher, and T. A. Lovell, "Use of Nonlinearities for Increased Observability in Relative Orbit Estimation," *AAS/AIAA Astrodynamics Specialist Conference*, 2015.

[8] S. Garg and A. Sinclair, "Initial Relative-Orbit Determination Using Second-Order Dynamics and Line-of-Sight Measurements," *AAS/AIAA Astrodynamics Specialist Conference*, 2015.

[9] J. Schmidt and T. A. Lovell, "Estimating Geometric Aspects of Relative Satellite Motion Using Angles-Only Measurements," *AAS/AIAA Astrodynamics Specialist Conference*, 2008.

[10] W. Clohessy and R. Wiltshire, "Terminal Guidance System for Satellite Rendezvous," *Journal of Aerospace Sciences*, Vol. 27, No. 9, 1960, pp. 653–658.

[11] G. Gaias, S. D'Amico, and J. S. Ardaens, "Angles-Only Navigation to a Noncooperative Satellite Using Relative Orbital Elements," *Journal of Guidance, Control, and Dynamics*, Vol. 37, No. 2, 2014, pp. 439–451.

[12] S. D'Amico, *Autonomous Formation Flying in Low Earth Orbit*. PhD thesis, Delft University, 2010.

[13] K. Yamanaka and F. Ankersen, "New State Transition Matrix for Relative Motion on an Arbitrary Elliptical Orbit," *Journal of Guidance, Control, and Dynamics*, Vol. 25, No. 1, 2002, pp. 60–66.

[14] K. Alfriend, S. Vadali, P. Gurfil, J. How, and L. Breger, *Spacecraft Formation Flying: Dynamics, Control, and Navigation*. Elsevier Astrodynamics Series, 2010.

[15] F. De Bruijn, E. Gill, and J. How, "Comparative Analysis of Cartesian and Curvilinear Clohessy–Wiltshire Equations," *Journal of Aerospace Engineering, Sciences and Applications*, Vol. 3, No. 2, 2011, pp. 1–15.

[16] P. A. Kuchment, *Floquet theory for partial differential equations*, Vol. 60. Birkhäuser, 2012.

[17] D.-W. Gim and K. T. Alfriend, "State transition matrix of relative motion for the perturbed noncircular reference orbit," *Journal of Guidance, Control, and Dynamics*, Vol. 26, No. 6, 2003, pp. 956–971.

[18] G. Gaias, J. S. Ardaens, and O. Montenbruck, "Model of J_2 Perturbed Satellite Relative Motion with Time-Varying Differential Drag," *Celestial Mechanics and Dynamical Astronomy*, Vol. 123, No. 4, 2015, pp. 411–433.

[19] O. Montenbruck, R. Kahle, S. D'Amico, and J. S. Ardaens, "Navigation and Control of the TanDEM-X Formation," *Journal of Astronautical Sciences*, Vol. 56, 2008, pp. 341–357.

[20] E. Gill, O. Montenbruck, and S. D'Amico, "Autonomous Formation Flying for the PRISMA Mission," *Journal of Spacecraft and Rockets*, Vol. 44, 2007, pp. 671–681.

[21] S. D'Amico, J. S. Ardaens, G. Gaias, H. Benninghoff, B. Schlepp, and J. L. Jorgensen, "Noncooperative Rendezvous Using Angles-Only Optical Navigation: System Design and Flight Results," *Journal of Guidance, Control, and Dynamics*, Vol. 36, No. 6, 2013, pp. 1576–1595.

[22] G. Gaias, J. S. Ardaens, and S. D'Amico, "The Autonomous Vision Approach Navigation and Target Identification (AVANTI) Experiment: Objectives and Design," *9th International ESA Conference on Guidance, Navigation, and Control Systems*, 2014.

[23] S. D'Amico and O. Montenbruck, "Proximity Operations of Formation Flying Spacecraft Using an Eccentricity/Inclination Vector Separation," *Journal of Guidance, Control, and Dynamics*, Vol. 29, No. 3, 2006, pp. 554–563.

[24] H. Schaub and J. L. Junkins, *Analytical Mechanics of Space Systems*. AIAA Education Series, 2003.

[25] J. R. Yim, J. L. Crassidis, and J. L. Junkins, "Autonomous Orbit Navigation of Two Spacecraft System Using Relative Line of Sight Vector Measurements," *AAS/AIAA Spaceflight Mechanics Conference*, 2004.

[26] B. Bingham and D. Geller, "Preliminary Orbit Determination for Orbital Rendezvous Using Gauss' Method," *AAS/AIAA Astrodynamics Specialist Conference*, 2007.

[27] R. Karimi, *Designing an Interplanetary Autonomous Spacecraft Navigation System Using Visible Planets*. PhD thesis, Texas A&M University, 2012.

[28] UT/CSR, "GRACE Gravity Field Model GGM01," tech. rep., University of Texas, Center for Space Research, 2003. http://www.csr.utexas.edu/grace/gravity/ggm01/GGM01Notes.pdf.

[29] L. G. Jacchia, "Revised static models of the thermosphere and exosphere with empirical profiles," *Res. Space Sci. Spec. Rep. 332*, Smithson. Astrophys. Observ Cambridge, Mass, 1971.

[30] O. Montenbruck and E. Gill, *Satellite Orbits- Models, Methods, and Applications*. Springer-Verlag, 2001.

[31] J. L. Jørgensen, T. Denver, M. Betto, and P. S. Jørgensen, "Microasc-a miniature star tracker," *Technical University of Denmark, Dept. of Measurement and Instrumentation*, 2001.

[32] S. Palo, G. Stafford, and A. Hoskins, "An agile multi-use nano star camera for constellation applications," 2013.

[33] O. Montenbruck, B. Nortier, and S. Mostert, "A Miniature GPS Receiver for Precise Orbit Determination of the Sunsat 2004 Micro-Satellite," *Proceedings of the 2004 National Technical Meeting of The Institute of Navigation*, 2001, pp. 636–642.